JACS
JOURNAL OF THE AMERICAN CHEMICAL SOCIETY
pubs.acs.org/JACS
Article

Combinatorial Studies of Palladium-Based Oxygen Reduction Electrocatalysts for Alkaline Fuel Cells

Yao Yang,[$] Guanyu Chen,[$] Rui Zeng, Andrés Molina Villarino, Francis J. DiSalvo, R. Bruce van Dover,* and Héctor D. Abruña*

Cite This: https://dx.doi.org/10.1021/jacs.9b13400 Read Online

ACCESS | Metrics & More | Article Recommendations | Supporting Information

ABSTRACT: Hydrogen fuel cells have emerged as promising, potentially renewable energy-based, energy conversion technologies for powering electric vehicles. However, the sluggish oxygen reduction reaction (ORR) at the cathode has remained a longstanding challenge and requires the design of nonplatinum electrocatalysts with high activity and, ideally, low cost. Here, we present a combinatorial study of Pd−Cu thin-film electrodes with well-defined composition and structures, prepared by magnetron sputtering, as a fast method for assessing the ORR activity of binary alloys. This represents a facile catalyst screening method, using replaceable glassy carbon disk electrodes, which enables the rapid and reliable evaluation of ORR activity using standard rotating disk electrode (RDE) measurements. Among nine Pd−Cu alloys, $Pd_{50}Cu_{50}$ was identified as the most promising composition for the ORR and employed as a target for nanoparticle synthesis. The PdCu nanoparticles, supported on carbon, achieved a mass-specific and surface-specific activity, 3 and 2.5 times, respectively, as high as Pd/C in 1 M KOH. PdCu/C further exhibited an impressive durability with only 3 and 13 mV negative shifts in the half-wave potential after 20000 and 100000 potential cycles, respectively. The combinatorial approach guiding the nanoparticle synthesis, described herein, provides an optimized high-throughput screening method for other binary or ternary alloys as fuel cell electrocatalysts.

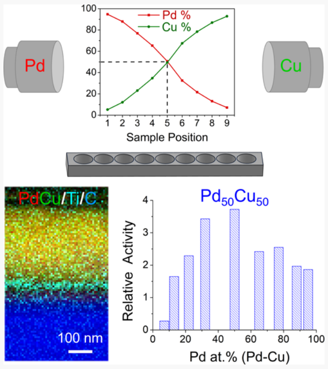

■ INTRODUCTION

As key renewable energy technologies, hydrogen fuel cells have gained increasing attention for their high energy conversion efficiency and low carbon emissions.[1,2] However, the oxygen reduction reaction (ORR) at the cathode has slow kinetics and typically requires a significant amount of expensive Pt (>0.2 g/kW) for a power density of >1 W/cm^2 in proton exchange membrane, or acidic, fuel cells (PEMFCs).[3−6] Therefore, the development of Pt-free ORR catalysts is critical for the implementation of PEMFCs. Among the alternatives to circumvent the use of Pt in PEMFCs, alkaline fuel cells have emerged as particularly promising since they enable the use of Pd and other non-Pt electrocatalysts for the ORR. Pd is the only transition metal with ORR activity comparable to Pt in alkaline media.[7] In addition, alloying Pd with lower-cost 3d-transition metals has been reported to be an effective strategy to tune the lattice parameter and electronic structure of Pd so as to enhance its ORR activity.[8−13] For example, Pd−Cu disordered alloys (solid solutions) were reported to be active ORR electrocatalysts in acidic media. While alloying a precious metal with a non-noble metal (e.g., PdCu) can increase activity, the non-noble metal often leaches (especially in acidic media) during potential cycles, which can contaminate the membrane and compromise performance.[14,15] In contrast, based on the Pourbaix diagram of Cu, Pd−Cu alloys can be thermodynamically more stable in alkaline media (pH = 13∼14), when compared to acidic media.[16] Despite extensive studies on Pd-based electrocatalysts, the electrocatalytic mechanism for the ORR in alkaline media has remained elusive. The fact that ORR electrocatalytic activity depends on particle composition, size, morphology, and surface and crystal structures, makes this task monumentally difficult. Additionally, nanoparticle studies often involve time-consuming trial-and-error synthetic procedures. Therefore, a systematic high-throughput combinatorial approach, with well-controlled morphology and structure, would be particularly beneficial for assessing and evaluating promising Pd-based candidate catalysts in a time-efficient manner.

Combinatorial synthesis and screening methods have enabled the efficient preparation of solid-state materials libraries. Previous developments have contributed to the discovery of new functional materials with dielectric,[17] magnetic,[18] superconducting,[19] and luminescent properties,[20] among others. Over the past two decades, significant progress has been made in the screening of electrocatalysts for fuel cell and water splitting applications. The pioneering work of

Received: December 12, 2019
Published: February 6, 2020

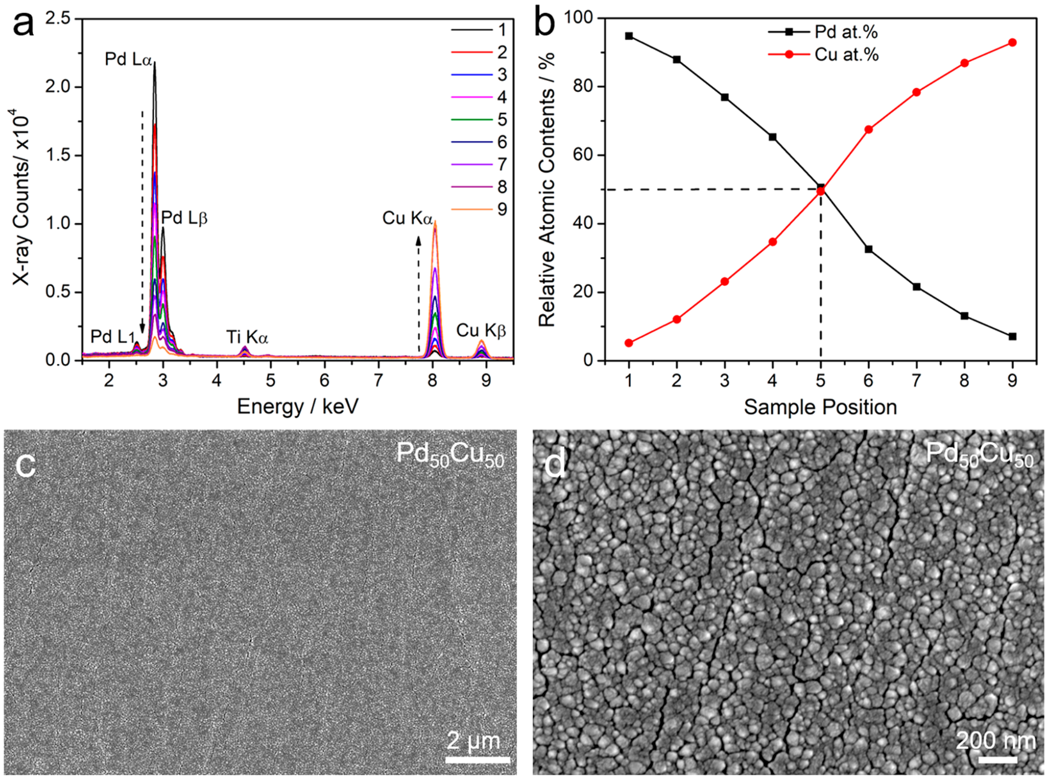

Figure 1. Elemental quantification of Pd−Cu thin-films. (a) EDX spectra of Pd−Cu thin films with sample positions from 1 to 9 (Pd-rich to Cu-rich). Pd L*α*,*β* and Cu K*α* edges were used for elemental quantification. The Ti signal came from the Ti adhesion layer. (b) Relative atomic contents of Pd and Cu (at. %) as a function of the sample position, which covers the range of Pd at. % from ∼95% to ∼5% with $Pd_{50}Cu_{50}$ in the middle. (c, d) SEM images of $Pd_{50}Cu_{50}$ showing a uniform film morphology and a domain size of around 100 nm.

Mallouk et al. employed inkjet printing and a subsequent borohydride reduction method to screen a broad range of binary, ternary, and quaternary precious metal electrocatalysts.[21] They developed a fluorescent acid−base indicator method to detect the concentration of protons, which were generated during the methanol oxidation reaction, and identified a composition of $Pt_{44}Ru_{41}Os_{10}Ir_5$ as the one with optimal activity. We recently employed a similar fluorescent-based method and synchrotron-based X-ray fluorescence (XRF) spectroscopy to screen Pt-M binary alloys (M included 18 different metals) and selected promising catalysts, such as $Pt_{65}Ru_{35}$.[22−24] Hillier et al. proposed scanning electrochemical microscopy (SECM) as a reliable technique to screen PtRu-based catalysts for hydrogen and methanol oxidation.[25,26] Bard et al. designed a piezo-based microarray dispenser to prepare Co-M binary alloy (M: Pd, Ag, Au) catalyst arrays for the ORR in acidic media and Fe_2O_3-based bimetallic oxide arrays for water oxidation and assessed their activity using SECM.[27,28] Russel et al. developed addressable multichannel array electrodes to study Pt−Ru alloys as CO-tolerant methanol oxidation electrocatalysts[29,30] and Pt−Pd−Au alloys for the ORR in acidic media.[31] Recently, Berlinguette et al. developed a photochemical metal−organic deposition (PMOD) method to prepare various amorphous Fe−Co−Ni trimetallic oxides for water oxidation.[32,33]

In the development of PEMFCs, the rotating disk electrode (RDE) technique has been widely used in research laboratories as the standard tool to evaluate electrocatalytic activity. In contrast, the aforementioned fluorescent-based and SECM techniques only provide indirect predictions/indications of potential activity. Multichannel array electrodes require delicate device fabrication and few of those results have translated into realistic activities in RDE measurements. There is clearly a need for a standard and reliable RDE platform for catalyst screening. Here, we report on a facile catalyst screening method using replaceable glassy carbon disk electrodes as the substrates, which enables the rapid and reliable evaluation of ORR activity using standard RDE measurements. We employed a high-throughput magnetron sputtering chamber to prepare binary Pd−Cu solid solution electrocatalyst thin films for the ORR in alkaline media. Among nine different compositions of Pd−Cu alloys, $Pd_{50}Cu_{50}$ (i.e., 1:1 molar ratio, or just PdCu) was found to be the most promising candidate. Following this guidance, and using an impregnation-reduction method, we further synthesized $Pd_{50}Cu_{50}$ nanoparticles which showed promising activity and durability in alkaline electrochemical systems.

■ RESULTS AND DISCUSSION

Magnetron sputtering has been employed as a powerful tool to prepare various Pd-based binary thin films (Figure S1). Sputtering is a physical vapor deposition (PVD) method in which the positively charged ions from an Ar plasma strike a negatively charged metal target(s) with enough kinetic energy to sputter surface atoms from the target(s). In magnetron sputtering, a localized magnetic field under the target guns aids in controlling the electron trajectory in space and concentrating the Ar plasma over the target. Thus, higher plasma densities and improved deposition rates are achieved. The ejected target atoms redeposit on a substrate to form a thin film. In this work, a custom-built magnetron sputtering system was used for the combinatorial preparation of Pd-based thin films (Figure S1a).[34] The sputtering chamber is composed of a sputtering gun on top, for depositing Ti adhesion layers, and three sputtering guns on the side for codepositing binary or ternary thin films. The sputtering chamber is pumped to high vacuum conditions ($<2 \times 10^{-6}$ Torr) before film deposition. Single-crystal Si wafers were used as the substrate for depositing films for XRD measurements. Polished glassy carbon (GC) electrodes (5 mm diameter) were loaded onto a homemade sample holder and used as substrates for electrochemical measurements (Pd−Cu/Ti/GC, Figure S1b,c). A maximum of nine electrodes could be loaded per batch and are labeled No. 1 to No. 9 from the position closer to the Pd and Cu targets, respectively. After film deposition, the Pd−Cu/Ti/GC electrodes were mounted into a replaceable disk setup for rotating disk electrode (RDE) measurements (Figure S1d).

Scanning electron microscopy (SEM) and energy dispersive X-ray (EDX) spectroscopy were employed to assess the surface morphology and chemical composition of the Pd−Cu thin films. As shown in Figure 1a, the EDX spectra of a series of Pd−Cu thin films exhibited a progressive compositional change from sample No. 1 to No. 9. The Pd Lα,β edges at around 2.8 keV showed a gradual decrease in the intensity while the Cu Kα,β edges at 8.0 and 8.9 keV increased, showing the inverse proportionality of the Pd and Cu at. % at different sample positions. The Ti Kα edge at 4.5 keV was also detected due to presence of the Ti adhesion layer under the films. The relative Pd at. % and Cu at. % were quantified based on the Pd L and Cu K edges using the Cliff-Lorimer equation.[35] The total elemental contents of Pd and Cu were set to 100%, and the relative errors (one standard deviation) were estimated to be 1−2%. As shown in Figure 1b, the Pd at. % smoothly decreased from 95% in sample No. 1 to 7% in sample No. 9. With the sputtering powers of the targets properly calibrated, one could achieve a $Pd_{50}Cu_{50}$ (Pd/Cu atomic ratio, 1:1) in sample No. 5 (indicated by dashed lines in Figure 1b). We observe a Pd or Cu concentration gradient of about 1 at. % per mm across the substrate, although the change was not perfectly linear (Figure 1b). The surface morphology of the thin films was characterized using SEM (Figure 1c). Over the field of view of 16 μm or larger, $Pd_{50}Cu_{50}$ showed highly uniform surface morphology without noticeable μm-sized agglomeration. The magnified SEM image of $Pd_{50}Cu_{50}$ in Figure 1d showed that the smooth surface was composed of metallic clusters with a size of approximately 100 nm. The surface morphologies of Pd-rich and Cu-rich films were also examined under SEM (Figure S2). $Pd_{77}Cu_{23}$ and $Pd_{22}Cu_{78}$ (estimated as Pd_3Cu and $PdCu_3$) exhibited a very homogeneous surface morphology over the μm-sized field of view (Figure S2a,c). When compared to $Pd_{50}Cu_{50}$, $Pd_{77}Cu_{23}$, and $Pd_{22}Cu_{78}$ exhibited a similar surface morphology with metallic clusters of around 100 nm (Figure S2b,d).

After examining the surface morphology and bulk compositions, we also characterized the structure and chemical compositions of cross sections of the thin films. The SEM image in Figure S3 presents the cross section of a $Pd_{50}Cu_{50}$/Ti/C sample. EDX mapping was employed to evaluate the elemental distribution in the cross section (Figure 2). The L edge of Pd and K edges of C, Ti, and Cu were used to construct the elemental maps. The elemental maps of C, Ti, Pd, and Cu provided a direct visualization of the layered structure of $Pd_{50}Cu_{50}$/Ti/C along the cross section (Figure 2b−e). In particular, the EDX map of Ti suggested a Ti adhesion layer with a thickness of around 50 nm (Figure 2c). The EDX maps of Pd and Cu indicated a catalyst layer of around 350 nm (Figure 2d,e). The composite map of Pd + Cu in Figure 2f showed a homogeneous elemental distribution of Pd and Cu, indicating the successful formation of a well-mixed binary alloy at the nanometer scale. The EDX map of PdCu on another region also confirmed the same observation of ∼50 nm Ti and ∼350 nm PdCu film thicknesses, respectively (Figure S4).

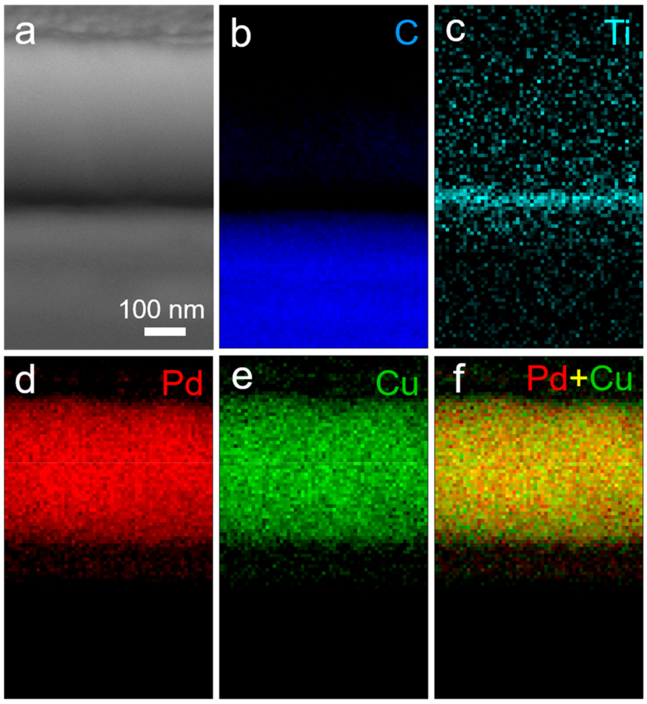

Figure 2. SEM image (a) and the corresponding EDX elemental maps of C (b), Ti (c), Pd (d), Cu (e), and the composite map of Pd + Cu (f) for a $Pd_{50}Cu_{50}$ thin film. The thicknesses of the Pd−Cu thin films and Ti underlayer were estimated to be about 350 and 50 nm, respectively. The uniform false color map in yellow in part f suggests a homogeneous elemental distribution of Pd and Cu.

The crystal structure of the Pd−Cu thin films was examined using X-ray diffraction (XRD). All nine Pd−Cu samples exhibited single-phase face centered cubic (fcc) solid solutions with characteristic peaks such as, (111), (200), and (220) (Figures S5 and S6). As the thin film compositions changed from the Pd-rich sample No. 1 to the Cu-rich sample No. 9, the diffraction peaks progressively shifted to higher 2θ angles due to the incorporation of Cu, with a smaller atomic size, into the Pd lattice. The Pd−Cu (111) peaks shifted to higher angles at higher Cu at. % with $Pd_{50}Cu_{50}$ (green lines) located right at the middle (Figure 3a). The lattice parameters of Pd−Cu thin films were calculated based on Bragg's equation (Figure 3a) and plotted as a function of Pd at. % (Figure 3b). The Pd−Cu thin films exhibited an excellent linear relation of the calculated lattice parameter as a function of Pd at. % with a linear fitting coefficient $R^2 = 0.993$ (Figure 3b). The fitted linear equation was calculated as $y = 0.0027x + 3.62$. The y-intercept (3.62 Å) at 0% of Pd is consistent with the lattice parameter of pure Cu (3.615 Å). The slope (0.0027 Å) is consistent with the theoretical percentage difference in the lattice parameters between Pd and Cu ((3.890−3.615 Å)/100 = 0.00275 Å). This represents compelling evidence that the Pd−Cu thin films formed solid solutions.

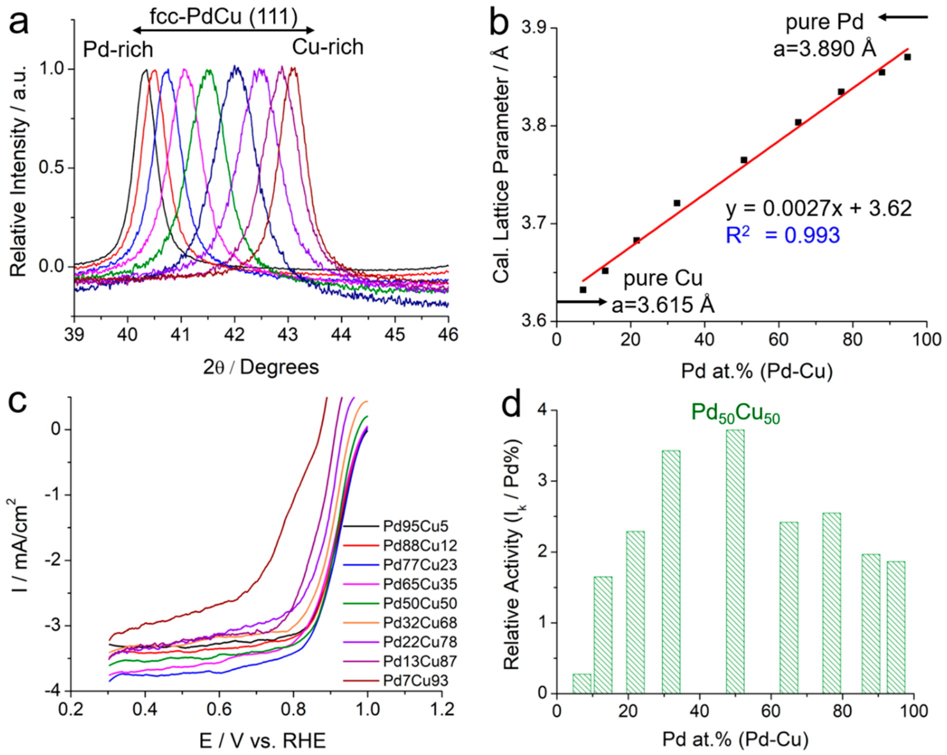

Figure 3. (a) XRD patterns of the (111) facets of Pd−Cu alloys. The composition progressively changed from Pd-rich to Cu-rich compositions, leading to the gradual peak shift to higher 2θ angles due to the incorporation of Cu (with a smaller atomic size) into the Pd lattice. (b) Lattice parameter of Pd−Cu thin films, calculated from (111) peaks as a function of the Pd at. %. The scatter plot was fitted into a linear expression of $y = 0.0027x + 3.62$ with a linearity of $R^2 = 0.993$. The y-intercept is the lattice parameter of Cu, and the slope is the percentile difference of lattice parameter between Pd and Cu. (c) ORR polarization profiles of Pd−Cu thin films at 5 mV/s and 1600 rpm in O_2-saturated 1 M KOH. (d) Relative ORR activity obtained by normalizing the kinetic current to the Pd at. % as a function of Pd at. % in the Pd−Cu thin films.

The Pd−Cu thin films were subsequently tested as electrocatalysts for the ORR in alkaline media. Pd−Cu/Ti/GC electrodes were loaded into the described replaceable disk electrode assembly for RDE measurements in 1 M KOH at a scan rate of 5 mV/s and a rotation rate of 1600 rpm. Relative to 0.1 M KOH, 1 M KOH is closer to the realistic OH^- concentration in practical membrane electrode assembly (MEA) tests.[36−38] It should be noted that, based on the Levich equation, the diffusion-limited current density, I_d, at 1600 rpm for the 4e$^-$ reduction of oxygen in O_2-saturated 0.1 M KOH and 1 M KOH should be around −5.5 and −3.6 mA/cm^2, respectively. I_d in 1 M KOH is smaller in magnitude since the O_2 solubility in 1 M KOH is only 70% of that in 0.1 M KOH.[39] As shown in Figure 3c, Pd−Cu thin films were able to achieve a I_d of around −3.5 mA/cm^2, suggesting the preponderance of the 4e$^-$ process of reducing O_2 completely to H_2O, instead of the 2e$^-$ process leading to hydrogen peroxide formation. Pd−Cu thin films with Pd at. % from 32% to 7% (Cu-rich alloys) exhibited I_d values lower than −3.5 mA/cm^2, indicating a larger contribution from hydrogen peroxide formation. Lowering the Pd at. % from 32% to 7% also caused a noticeable decrease in the half-wave potential ($E_{1/2}$) of 31 mV. To quantitatively assess the activity of the various Pd−Cu thin films, the kinetic current (I_k) at 0.9 V was calculated, based on the Koutecký-Levich equation, and normalized to the relative Pd at. %. As previously shown, the Pd−Cu thin films were homogeneously mixed on the surface, as evidenced by the SEM-EDX maps (Figure 2f). Therefore, the relative Pd at. % can be used as representing the relative coverage of Pd on the surface. Normalizing the I_k to Pd at. % can, thus, represent the relative intrinsic activity per Pd site. As shown in Figure 3d, the relative activity of various Pd−Cu thin films followed a *"volcano plot"* with an optimal activity at $Pd_{50}Cu_{50}$. The relative activity of $Pd_{50}Cu_{50}$ was about twice that of the nearly pure Pd film ($Pd_{95}Cu_5$). Further increases of the Cu at. % above 50% caused a gradual decay of the relative activity and, eventually, a significantly low activity at Pd_7Cu_{93} (only 15% of the relative activity of $Pd_{95}Cu_5$). Cyclic voltammetric (CV) profiles of Pd−Cu thin films suggested that lowering the Pd content from $Pd_{88}Cu_{12}$ to $Pd_{50}Cu_{50}$ and $Pd_{13}Cu_{87}$ caused the hydrogen region (0.1−0.2 V) to be suppressed as a result of having fewer Pd sites on the surface. (Figure S7). Lower Pd content (i.e., higher Cu at. %) was also associated with larger reduction peaks near 0.7 V, which was presumably due to the formation of larger amounts of Cu oxide during the previous positive scan. In summary, the RDE measurements indicated that $Pd_{50}Cu_{50}$ is a promising composition for PdCu nanoparticles for the ORR in alkaline media. This is consistent with an optimal value of the oxygen binding energy of Pd−Cu alloys at 1:1 Pd/Cu ratio, as reported in previous DFT calculations.[40]

Following the thin film screening, Pd and PdCu nanoparticles, supported on carbon, were synthesized by an impregnation-reduction method using either metal chlorides or nitrates as precursors (Figure S8). As shown in the phase diagram of PdCu (Figure S9), PdCu with a molar ratio of 1:1 is located at the edge between the single-phase PdCu and a multiphase region, indicating that its chemical synthesis requires a delicate control of the precursor types and reaction conditions. When Pd and Cu chlorides were used as precursors and reduced at 800 °C for 12 h in forming gas, the synthesized PdCu/C exhibited a single-phase ordered structure (o-PdCu/C, CsCl-type, *Pm*-3m) with characteristic (100), (110), etc. diffraction peaks. (Figure 4). The domain size of the PdCu nanoparticles was estimated to be around 25 nm based on the Scherrer equation. Lowering the reaction time or temperature caused significant phase segregation (Figure S10). As a comparison, Pd/C, with a face centered cubic (fcc) phase, was synthesized at 800 °C for 4 h to achieve a similar particle size and surface area, relative to PdCu/C (Figure 4). When Pd and Cu nitrates were employed to synthesize PdCu alloy nanoparticles, the XRD patterns showed a dramatic difference in the crystal structure, when compared to o-PdCu/C (Figure S11). Reaction temperatures that were too low, under forming gas (e.g., 400 °C), resulted in the formation of a mixture of elemental Pd and Cu as well as Pd−Cu disordered alloys. However, reaction temperatures that were too high (e.g., 900 °C) resulted in mixed phases of Pd-rich and Cu-rich alloys (green lines). Even the optimized reaction conditions of 800 °C for 12 h still led to the formation of asymmetrical diffraction peaks in the PdCu disordered alloys (cyan lines), indicating multiphased nanoparticles.

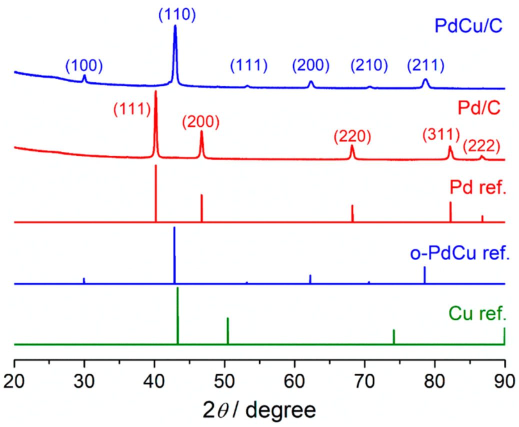

Figure 4. XRD patterns of PdCu and Pd nanoparticles supported on carbon with the references of Pd, Cu, and o-PdCu (o-PdCu, PDF # 04-015-2413).

To this end, single-phase ordered PdCu/C was synthesized from Pd and Cu chloride precursors at 800 °C for 12 h. It has been reported that Pd and Pt-based intermetallics, or ordered phases, can effectively mitigate the leaching problem of 3d metals and can also exhibit enhanced durability, relative to their disordered counterparts.[5,6,8,41−46] Therefore, we focused on the synthesized o-PdCu/C for further structural and electrochemical characterization.

The microstructure of o-PdCu/C was analyzed using a high-angle annular dark-field scanning/transmission electron microscope (HAADF-S/TEM). o-PdCu/C exhibited a uniform size distribution of PdCu nanoparticles on the carbon (Figure 5a). Statistical analysis of around 500 PdCu nanoparticles resulted in a particle size distribution (PSD) of 40 ± 7 nm (Figures 5b

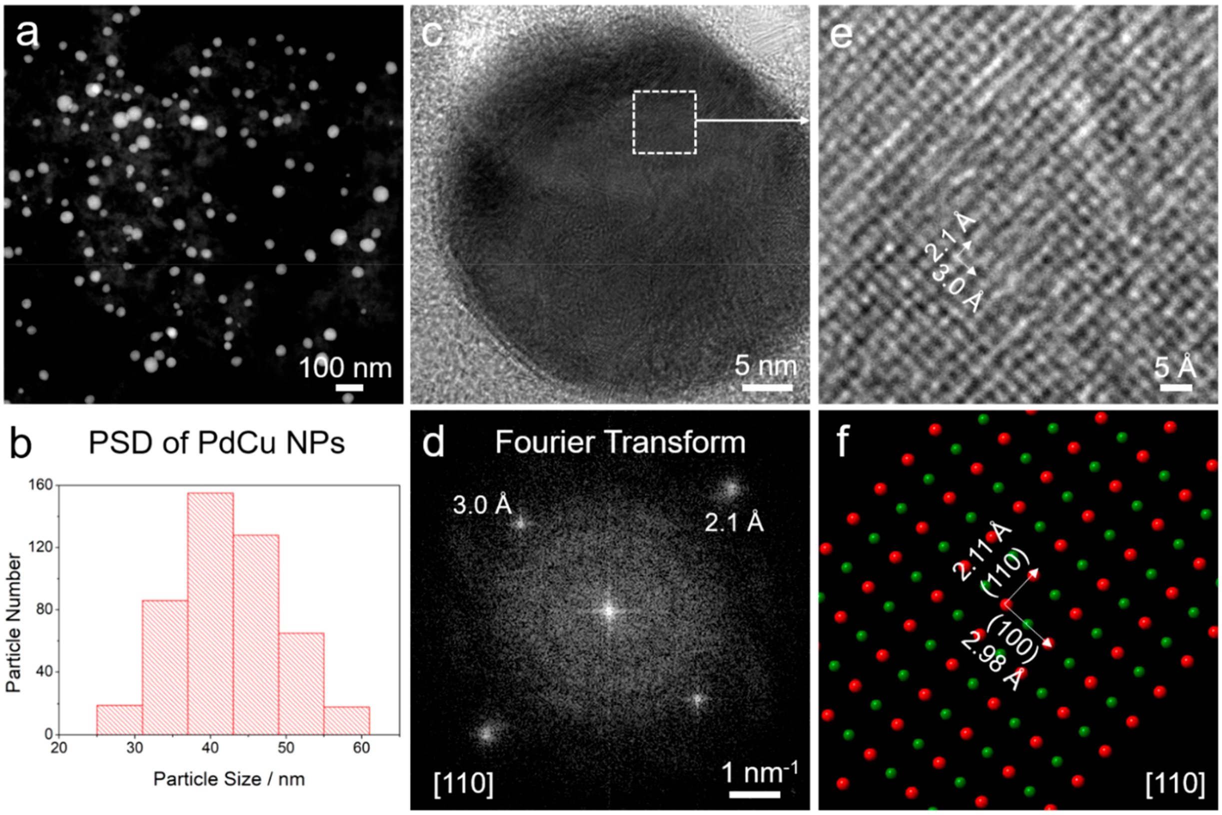

Figure 5. S/TEM images of PdCu nanoparticles supported on carbon. (a, b) HAADF-STEM images of PdCu/C and particle size distribution of around 500 PdCu nanoparticles. (c, d) A single crystal PdCu nanoparticle with the corresponding Fourier transform on the [110] zone axis. (e, f) Atomic-scale TEM image of PdCu nanoparticles showing the periodic rectangular 2D unit cells with the same *d*-spacings of 3.0 and 2.1 Å, which is consistent with the theoretical values of (110) and (100) facets, respectively, based on the crystal model of ordered PdCu in part f (PDF # 04−015−2413).

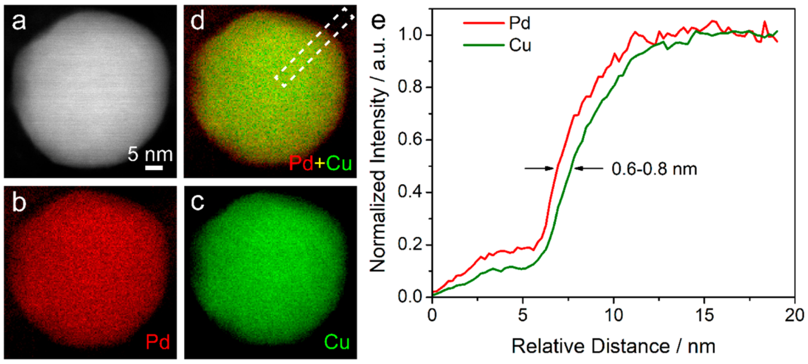

Figure 6. (a) STEM image of a PdCu nanoparticle and (parts b–d) the corresponding EELS elemental maps of Pd (b), Cu (c), and Pd + Cu, showing a thin Pd shell (red) on the surface (d). (e) EELS line scan profile extracted from the dashed box in part d, indicating a 0.6–0.8 nm Pd shell (2–3 atomic layers).

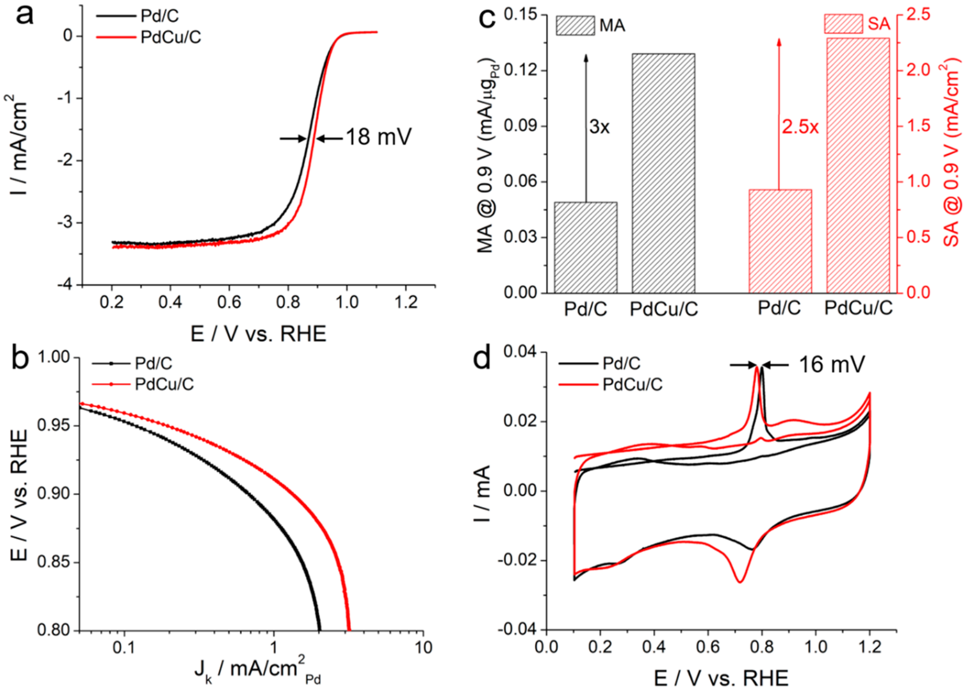

Figure 7. ORR activity of PdCu/C and Pd/C. (a) ORR polarization profiles of Pd/C and PdCu/C in O_2-saturated 1 M KOH at 1600 rpm and 5 mV/s. (b) Tafel plots of Pd/C and PdCu/C. (c) MA and SA of Pd/C and PdCu/C at 0.9 V vs RHE. MA was normalized to the Pd loading and SA was normalized to the ECSA from CO stripping results. (c) CO stripping measurements of Pd/C and PdCu/C at 10 mV/s. The CO dosing potential was 0.1 V.

and S12). This differs from the average domain size of 25 nm calculated from the XRD, suggesting that these nanoparticles have multiple domains. As a comparison, Pd/C, synthesized at 800 °C for 4 h, showed a similar narrow PSD of 50 ± 9 nm (Figure S13). The atomic-scale bright field (BF) TEM image and the corresponding Fourier transform of the o-PdCu showed a single-crystal structure on the [110] zone axis with two perpendicular *d*-spacings of 3.0 and 2.1 Å, respectively (Figure 5c,d). The enlarged TEM image in Figure 5e directly visualized the ordered structure with periodic rectangular 2D unit cells and the same *d*-spacings as anticipated. The *d*-spacings of 3.0 and 2.1 Å were assigned to the (100) and (110) lattice planes, consistent with the theoretical values of 2.98 and 2.11 Å in the crystal model on the same zone axis of ordered PdCu (PDF # 04-015-2413, Figure 5f). The chemical composition of o-PdCu/C was examined using STEM equipped with electron energy loss spectroscopy (EELS). As shown in Figure 6a–d, EELS elemental maps of Pd (red), Cu (green) and composite map of Pd + Cu indicated that the PdCu core (yellow) was surrounded by a thin Pd shell (red) on the surface. The EELS line profile in Figure 6e, extracted from dashed box in Figure 6d, suggested a Pd shell of 0.6–0.8 nm, corresponding to 2–3 atomic layers. Such a thin Pd-rich shell, on the surface of PdCu, may serve as a protection layer to effectively mitigate possible Cu leaching, enhance catalytic activity, and improve catalyst durability.

After detailed structural investigations, the ORR activities of PdCu/C and Pd/C were evaluated with a catalyst ink deposited on a GC electrode in an RDE system in O_2-saturated 1 M KOH. The ORR polarization profiles in Figure 7a showed that the $E_{1/2}$ of PdCu/C was 0.886 V, 18 mV more positive than that of Pd/C (0.868 V), corresponding to a significant increase in ORR activity. Tafel plots of PdCu/C exhibited a smaller Tafel slope of 36 mV/dec in the early

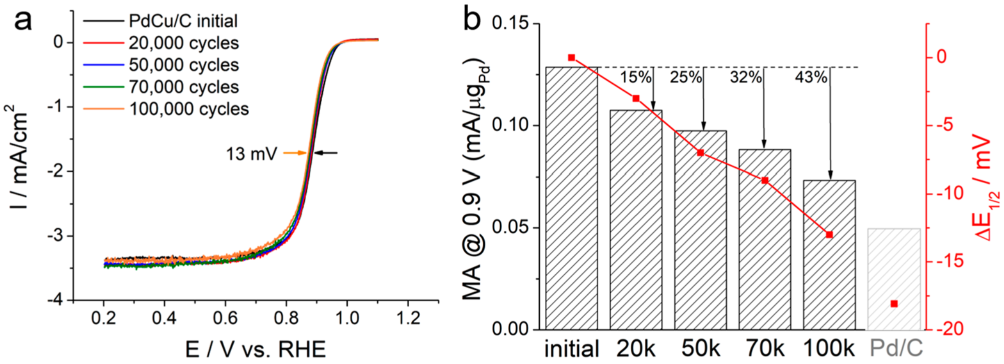

Figure 8. Durability tests of PdCu/C in O_2-saturated 1 M KOH following an accelerated aging protocol: 0.6−1.0 V at 100 mV/s. (a) ORR polarization profiles of PdCu/C at the initial state and after 20000 to 100000 accelerated cycles. The $E_{1/2}$ shifted to lower potentials by only 13 mV after 100000 cycles. (b) MA at 0.9 V (left y-axis) and $\triangle E_{1/2}$ (right y-axis) at the initial state and after durability cycles. $\triangle E_{1/2}$ was calculated based on the difference from the $E_{1/2}$ of PdCu/C at the initial state (0.886 V). The MA of PdCu/C only showed a 15% loss after 20k cycles and still surpassed the performance of Pd/C (at the initial state) after 100k cycles.

kinetically controlled region (0.96−0.94 V), relative to Pd/C (42 mV/dec), indicating a smaller overpotential required to achieve the same kinetic current change (Figures 7b and S14). The mass-specific activity (MA) and surface-specific activity (SA) at 0.9 V were calculated to quantitatively assess electrocatalytic activity, by normalizing the kinetic current to the mass loading of Pd and electrochemical surface area (ECSA) calculated from CO stripping measurements, respectively (Figure 7c,d). The MA of PdCu/C at 0.9 V was 0.13 mA/μg_{Pd}, 3 times as high as Pd/C. The SA of PdCu/C at 0.9 V was 2.3 mA/cm^2_{Pd}, 2.5 times as high as Pd/C (Figure 7c). The superior ORR activity of PdCu/C, relative to Pd/C, was likely due to the lattice contraction (resulting in a strained layer) and weakened oxygen adsorption energy on the Pd lattice caused by the incorporation of Cu.[7,40] CO stripping measurements showed that PdCu/C had an ECSA of 54 cm^2/mg_{Pd}, comparable to that of Pd/C (50 cm^2/mg_{Pd}) (Figure 7d), which matched well with their similar particle sizes from TEM images (40 ± 7 and 50 ± 9 nm, respectively). PdCu/C showed a CO stripping peak potential of 0.781 V, which represents a 16 mV negative shift, relative to Pd/C, indicating a more CO-tolerant behavior, which would benefit the practical fuel cells operating in air.[2,3]

Finally, in order to implement a non-Pt cathode for practical alkaline fuel cells, ORR electrocatalysts need to not only achieve high initial ORR activity, but also exhibit long-term durability.[1−3] Benefiting from the stable ordered structure and enhanced stability of Cu in alkaline media (Figure S15), PdCu/C exhibited remarkable durability during prolonged potential cycles (Figure 8). PdCu/C showed a negligible activity decay with $\triangle E_{1/2}$ values of only 3 and 8 mV after 20000 and 50000 cycles from 0.6 to 1.0 V at 100 mV/s, respectively (Figure 8a,b). Concomitantly, the MA of PdCu/C at 0.9 V decreased only by 15% and 25%, respectively, after the same number of scans (Figure 8b). After extended testing (100000 cycles, about 220 h), the PdCu/C catalyst showed an unprecedentedly low $\triangle E_{1/2}$ of 13 mV and a MA retention of 57%, which still surpassed the initial performance of Pd/C ($\triangle E_{1/2}$ of 18 mV, MA marked in the gray histogram in Figure 8b). The progressive decay in activity during potential cycles was likely due to a decrease of the ECSA from particle aggregation/sintering over long-term cycles as evidenced by CO stripping (Figure S16).

In summary, we report on a combinatorial approach to prepare Pd-based thin films with well-controlled surface morphology and composition. $Pd_{50}Cu_{50}$ was identified as a promising candidate for nanoparticle synthesis. PdCu nanoparticles supported on carbon exhibited a significantly enhanced ORR activity, relative to Pd/C with a similar surface area. More importantly, PdCu/C was found to have remarkable durability up to 100000 cycles, with a higher mass activity and half-wave potential, when compared to pure and fresh Pd. This facile thin-film preparation method, used as a guideline for nanoparticle synthesis, can serve as a high-throughput approach for the rational design of other multimetallic alloys. Improvements on the synthesis of ordered Pd-based alloys, with smaller particle sizes under lower reaction temperature, are also important to further improve the mass activity of these nanoscale catalysts for practical fuel cell applications.

■ ASSOCIATED CONTENT

Supporting Information

The Supporting Information is available free of charge at https://pubs.acs.org/doi/10.1021/jacs.9b13400.

Thin-film preparation by magnetron sputtering, structural characterizations, electrochemical measurements, Pd-Cu nanoparticle synthesis (PDF)

■ AUTHOR INFORMATION

Corresponding Authors

R. Bruce van Dover − *Department of Materials Science and Engineering, Cornell University, Ithaca, New York 14853, United States*; Email: vandover@cornell.edu

Héctor D. Abruña − *Department of Chemistry and Chemical Biology, Cornell University, Ithaca, New York 14853, United States*; orcid.org/0000-0002-3948-356X; Email: hda1@cornell.edu

Authors

Yao Yang − *Department of Chemistry and Chemical Biology, Cornell University, Ithaca, New York 14853, United States*; orcid.org/0000-0003-0321-3792

Guanyu Chen − *Department of Materials Science and Engineering, Cornell University, Ithaca, New York 14853, United States*

Rui Zeng − *Department of Chemistry and Chemical Biology, Cornell University, Ithaca, New York 14853, United States;* orcid.org/0000-0002-7577-767X

Andrés Molina Villarino − *Department of Chemistry and Chemical Biology, Cornell University, Ithaca, New York 14853, United States*

Francis J. DiSalvo − *Department of Chemistry and Chemical Biology, Cornell University, Ithaca, New York 14853, United States*

Complete contact information is available at: https://pubs.acs.org/10.1021/jacs.9b13400

Author Contributions

[$]Y.Y. and G.C. contributed equally to this work.

Notes

The authors declare no competing financial interest.

■ ACKNOWLEDGMENTS

This work was primarily supported by the Center for Alkaline-Based Energy Solutions (CABES), an Energy Frontier Research Center (EFRC) program supported by the U.S. Department of Energy, under grant DE-SC0019445. This work made use of S/TEM facilities at the Cornell Center for Materials Research (CCMR) which are supported through the National Science Foundation Materials Research Science and Engineering Center (NSF MRSEC) program (DMR-1719875). We thank Marc Murphy for the early help in magnetron sputtering, and Yin Xiong, Abby Van Wassen, and Elliot Padgett for helpful discussions.

■ REFERENCES

(1) Debe, M. K. Electrocatalyst Approaches and Challenges for Automotive Fuel Cells. *Nature* **2012**, *486*, 43−51.

(2) Gasteiger, H. A.; Kocha, S. S.; Somali, B.; Wagner, F. T. Activity Benchmarks and Requirements for Pt, Pt-alloy, and non-Pt Oxygen Reduction Catalysts for PEMFCs. *Appl. Catal., B* **2005**, *56*, 9−35.

(3) Ayers, K.; Dalton, L.; Roemer, A.; Carter, B.; Niedzwiecki, M.; Manco, J.; Anderson, E.; Capuano, C.; Wang, C.-Y.; Zhao, W. High Performance, Low Cost Hydrogen Generation from Renewable Energy. U.S. Department of Energy Technical Report. 2014, DOI: DOI: 10.2172/1117668.

(4) Papageorgopoulos, D. 2019 Annual Merit Review and Peer Evaluation Meeting in Fuel Cells Program Area. U.S. Department of Energy, Washington, DC, April 2019.

(5) Wang, D.; Xin, H. L.; Hovden, R.; Wang, H.; Yu, Y.; Muller, D. A.; DiSalvo, F. J.; Abruña, H. D. Structurally Ordered Intermetallic Platinum-Cobalt Core-Shell Nanoparticles with Enhanced Activity and Stability as Oxygen Reduction Electrocatalysts. *Nat. Mater.* **2013**, *12*, 81−87.

(6) Xiong, Y.; Yang, Y.; DiSalvo, F. J.; Abruña, H. D. Pt-Decorated Composition-Tunable Pd−Fe@Pd/C Core−Shell Nanoparticles with Enhanced Electrocatalytic Activity toward the Oxygen Reduction Reaction. *J. Am. Chem. Soc.* **2018**, *140*, 7248−7255.

(7) Lima, F.; Zhang, J.; Shao, M.; Sasaki, K.; Vukmirovic, M.; Ticianelli, E.; Adzic, R. Catalytic Activity−d-Band Center Correlation for the O_2 Reduction Reaction on Platinum in Alkaline Solutions. *J. Phys. Chem. C* **2007**, *111*, 404−410.

(8) Yang, Y.; Xiao, W.; Feng, X.; Xiong, Y.; Gong, M.; Shen, T.; Lu, Y.; Abruña, H. D.; Wang, D. Golden Palladium Zinc Ordered Intermetallics as Oxygen Reduction Electrocatalysts. *ACS Nano* **2019**, *13*, 5968−5974.

(9) Jiang, G.; Zhu, H.; Zhang, X.; Shen, B.; Wu, L.; Zhang, S.; Lu, G.; Wu, Z.; Sun, S. Core/Shell Face-Centered Tetragonal FePd/Pd Nanoparticles as an Efficient Non-Pt Catalyst for the Oxygen Reduction Reaction. *ACS Nano* **2015**, *9*, 11014−11022.

(10) Wang, D.; Xin, H. L.; Wang, H.; Yu, Y.; Rus, E.; Muller, D. A.; DiSalvo, F. J.; Abruña, H. D. Facile synthesis of carbon-supported Pd−Co core−shell nanoparticles as oxygen reduction electrocatalysts and their enhanced activity and stability with monolayer Pt decoration. *Chem. Mater.* **2012**, *24*, 2274−2281.

(11) Xiao, W.; Cordeiro, M. A. L.; Gong, M.; Han, L.; Wang, J.; Bian, C.; Zhu, J.; Xin, H. L.; Wang, D. Optimizing the ORR activity of Pd based nanocatalysts by tuning their strain and particle size. *J. Mater. Chem. A* **2017**, *5*, 9867−9872.

(12) Luo, L.; Zhu, F.; Tian, R.; Li, L.; Shen, S.; Yan, X.; Zhang, J. Composition-Graded Pd_xNi_{1-x} Nanospheres with Pt Monolayer Shells as High-Performance Electrocatalysts for Oxygen Reduction Reaction. *ACS Catal.* **2017**, *7*, 5420−5430.

(13) Shao, M.; Shoemaker, K.; Peles, A.; Kaneko, K.; Protsailo, L. Pt Monolayer on Porous Pd-Cu Alloys as Oxygen Reduction Electrocatalysts. *J. Am. Chem. Soc.* **2010**, *132*, 9253−9255.

(14) Wang, X.; Kariuki, N.; Vaughey, J. T.; Goodpaster, J.; Kumar, R.; Myers, D. J. Bimetallic Pd−Cu Oxygen Reduction Electrocatalysts. *J. Electrochem. Soc.* **2008**, *155*, B602−609.

(15) Xu, C.; Zhang, Y.; Wang, L.; Xu, L.; Bian, X.; Ma, H.; Ding, Y. Nanotubular Mesoporous PdCu Bimetallic Electrocatalysts toward Oxygen Reduction Reaction. *Chem. Mater.* **2009**, *21*, 3110−3116.

(16) Beverskog, B.; Puigdomenech, I. Revised Pourbaix Diagrams for Copper at 25 to 300 °C. *J. Electrochem. Soc.* **1997**, *144*, 3476−3483.

(17) van Dover, R. B.; Schneemeyer, L. F.; Fleming, R. M. Discovery of a Useful Thin-Film Dielectric Using a Composition-Spread Approach. *Nature* **1998**, *392*, 162−164.

(18) Briceno, G.; Chang, H.; Sun, X.; Schultz, P. G.; Xiang, X.-D. A Class of Cobalt Oxide Magnetoresistance Materials Discovered with Combinatorial Synthesis. *Science* **1995**, *270*, 273−275.

(19) Xiang, X.-D.; Sun, X.; Briceno, G.; Lou, Y.; Wang, K.-A.; Chang, H.; Wallace-Freedman, W. G.; Chen, S.-W.; Schultz, P. G. A Combinatorial Approach to Materials Discovery. *Science* **1995**, *2268*, 1738−1740.

(20) Danielson, E.; Golden, J. H.; McFarland, E. W.; Reaves, C. M.; Weinberg, W. H.; Wu, X.-D. A Combinatorial Approach to the Discovery and Optimization of Luminescent Materials. *Nature* **1997**, *389*, 944−948.

(21) Reddington, E.; Sapienza, A.; Gurau, B.; Viswanathan, R.; Sarangapani, S.; Smotkin, E. S.; Mallouk, T. E. Combinatorial Electrochemistry: A Highly Parallel, Optical Screening Method for Discovery of Better Electrocatalysts. *Science* **1998**, *280*, 1735−1737.

(22) Tague, M. E.; Gregoire, J. M.; Legard, A.; Smith, E.; Dale, D.; Hennig, R.; DiSalvo, F. J.; van Dover, R. B.; Abruña, H. D. High Throughput Thin Film Pt-M Alloys for Fuel Electrooxidation: Low Concentrations of M (M = Sn, Ta, W, Mo, Ru, Fe, In, Pd, Hf, Zn, Zr, Nb, Sc, Ni, Ti, V, Cr, Rh). *J. Electrochem. Soc.* **2012**, *159*, F880−F887.

(23) Gregoire, J. M.; Tague, M. E.; Cahen, S.; Khan, S.; Abruña, H. D.; DiSalvo, F. J.; van Dover, R. B. Improved Fuel Cell Oxidation Catalysis in $Pt_{1-x}Ta_x$. *Chem. Mater.* **2010**, *22*, 1080−1087.

(24) Prochaska, M.; Jin, J.; Rochefort, D.; Zhuang, L.; DiSalvo, F. J.; Abruña, H. D.; van Dover, R. B. High Throughput Screening of Electrocatalysts for Fuel Cell Applications. *Rev. Sci. Instrum.* **2006**, *77*, No. 054104.

(25) Jayaraman, S.; Hillier, A. C. Screening the Reactivity of Pt_xRu_y and $Pt_xRu_yMo_z$ Catalysts toward the Hydrogen Oxidation Reaction with the Scanning Electrochemical Microscope. *J. Phys. Chem. B* **2003**, *107*, 5221−5230.

(26) Jayaraman, S.; Hillier, A. C. Construction and Reactivity Screening of a Surface Composition Gradient for Combinatorial Discovery of Electro-Oxidation Catalysts. *J. Comb. Chem.* **2004**, *6*, 27−31.

(27) Fernandez, J. L.; Walsh, D. A.; Bard, A. J. Thermodynamic Guidelines for the Design of Bimetallic Catalysts for Oxygen Electroreduction and Rapid Screening by Scanning Electrochemical Microscopy. M-Co (M: Pd, Ag, Au). *J. Am. Chem. Soc.* **2005**, *127*, 357−365.

(28) Lee, J.; Ye, H.; Pan, S.; Bard, A. J. Screening of Photocatalysts by Scanning Electrochemical Microscopy. *Anal. Chem.* **2008**, *80*, 7445−7450.

(29) Strasser, P.; Fan, Q.; Devenney, M.; Weinberg, W. H.; Liu, P.; Nørskov, J. K. High Throughput Experimental and Theoretical Predictive Screening of Materials − A Comparative Study of Search Strategies for New Fuel Cell Anode Catalysts. *J. Phys. Chem. B* **2003**, *107*, 11013.

(30) Smotkin, E. S.; Jiang, J.; Nayar, A.; Liu, R. High-Throughput Screening of Fuel Cell Electrocatalysts. *Appl. Surf. Sci.* **2006**, *252*, 2573−2579.

(31) Guerin, S.; Hayden, B. E.; Lee, C. E.; Mormiche, C.; Russell, A. E. High-Throughput Synthesis and Screening of Ternary Metal Alloys for Electrocatalysis. *J. Phys. Chem. B* **2006**, *110*, 14355−14362.

(32) Smith, R. D. L.; Prévot, M. S.; Fagan, R. D.; Zhang, Z.; Sedach, P. A.; Siu, M. K. J.; Trudel, S.; Berlinguette, C. P. Photochemical Route for Accessing Amorphous Metal Oxide Materials for Water Oxidation Catalysis. *Science* **2013**, *340*, 60−63.

(33) Smith, R. D. L.; Prévot, M. S.; Fagan, R. D.; Trudel, S.; Berlinguette, C. P. Water Oxidation Catalysis: Electrocatalytic Response to Metal Stoichiometry in Amorphous Metal Oxide Films Containing Iron, Cobalt, and Nickel. *J. Am. Chem. Soc.* **2013**, *135*, 11580−11586.

(34) Gregoire, J. M.; van Dover, R. B.; Jin, J.; DiSalvo, F. J.; Abruna, H. D. Getter Sputtering System for High-Throughput Fabrication of Composition Spreads. *Rev. Sci. Instrum.* **2007**, *78*, No. 072212.

(35) Cliff, G.; Lorimer, G. W. The Quantitative Analysis of Thin Specimens. *J. Microsc.* **1975**, *103*, 203−207.

(36) Peng, H.; Li, Q.; Hu, M.; Xiao, L.; Lu, J.; Zhuang, L. Alkaline Polymer Electrolyte Fuel Cells Stably Working at 80 °C. *J. Power Sources* **2018**, *390*, 165−167.

(37) Yang, Y.; Peng, H.; Xiong, Y.; Li, Q.; Lu, J.; Xiao, L.; DiSalvo, F. J.; Zhuang, L.; Abruña, H. D. High-Loading Composition-Tolerant Co−Mn Spinel Oxides with Performance beyond 1 W/Cm^2 in Alkaline Polymer Electrolyte Fuel Cells. *ACS Energy Lett.* **2019**, *4*, 1251−1257.

(38) Yang, Y.; Wang, Y.; Xiong, Y.; Huang, X.; Shen, L.; Huang, R.; Wang, H.; Pastore, J. P.; Yu, S. H.; Xiao, L.; Brock, J. D.; Zhuang, L.; Abruña, H. D. In Situ X-Ray Absorption Spectroscopy of a Synergistic Co-Mn Oxide Catalyst for the Oxygen Reduction Reaction. *J. Am. Chem. Soc.* **2019**, *141*, 1463−1466.

(39) Davis, R. E.; Horvath, G. L.; Tobias, C. W. The Solubility and Diffusion Coefficient of Oxygen in Potassium Hydroxide Solutions. *Electrochim. Acta* **1967**, *12*, 287−297.

(40) Tang, W.; Zhang, L.; Henkelman, G. Catalytic Activity of Pd/Cu Random Alloy Nanoparticles for Oxygen Reduction. *J. Phys. Chem. Lett.* **2011**, *2*, 1328−1331.

(41) Sra, A.; Schaak, R. Synthesis of Atomically Ordered AuCu and $AuCu_3$ Nanocrystals from Bimetallic Nanoparticle Precursors. *J. Am. Chem. Soc.* **2004**, *126*, 6667−6672.

(42) Cable, R.; Schaak, R. Solution Synthesis of Nanocrystalline M-Zn (M: Pd, Au, Cu) Intermetallic Compounds via Chemical Conversion of Metal Nanoparticle Precursors. *Chem. Mater.* **2007**, *19*, 4908−4104.

(43) Wang, D.; Liu, S.; Wang, J.; Lin, R.; Kawasaki, M.; Rus, E.; Silberstein, K. E.; Lowe, M. A.; Lin, F.; Nordlund, D.; Liu, H.; Muller, D. A.; Xin, H. L.; Abruña, H. D. Spontaneous Incorporation of Gold in Palladium-Based Ternary Nanoparticles Makes Durable Electrocatalysts for Oxygen Reduction Reaction. *Nat. Commun.* **2016**, *7*, 11941.

(44) Zhu, J.; Yang, Y.; Chen, L.; Xiao, W.; Liu, H.; Abruña, H. D.; Wang, D. Copper-Induced Formation of Structurally Ordered Pt−Fe−Cu Ternary Intermetallic Electrocatalysts with Tunable Phase Structure and Improved Stability. *Chem. Mater.* **2018**, *30*, 5987−5995.

(45) Xiong, Y.; Xiao, L.; Yang, Y.; DiSalvo, F. J.; Abruña, H. D. High-Loading Intermetallic Pt_3Co/C Core−Shell Nanoparticles as Enhanced Activity Electrocatalysts toward the Oxygen Reduction Reaction (ORR). *Chem. Mater.* **2018**, *30*, 1532−1539.

(46) Xiao, W.; Lei, W.; Gong, M.; Xin, H. L.; Wang, D. Recent Advances of Structurally Ordered Intermetallic Nanoparticles for Electrocatalysis. *ACS Catal.* **2018**, *8*, 3237−3256.